

Polar stratospheric nitric acid depletion surveyed from a decadal dataset of IASI total columns

Catherine Wespes^{1,a,*}, Gaetane Ronsmans^{1,a}, ~~Catherine Wespes^{1,a,*}~~, Lieven Clarisse¹, Susan Solomon², Daniel Hurtmans¹, Cathy Clerbaux^{1,3}, and Pierre-François Coheur¹

¹Université libre de Bruxelles (ULB), Spectroscopy, Quantum Chemistry and Atmospheric Remote Sensing (SQUARES), Brussels, Belgium

²Department of Earth, Atmospheric and Planetary Sciences, Massachusetts Institute of Technology, Cambridge, Massachusetts, USA

³LATMOS/IPSL, Sorbonne Université, UVSQ, CNRS, Paris, France

^a Co-first authors

* Corresponding author: Catherine Wespes (catherine.wespes@ulb.be)

Abstract

In this paper, we exploit the first 10-year data-record (2008-2017) of nitric acid (HNO₃) total columns measured by the IASI-A/Metop infrared sounder, characterized by an exceptional daily sampling and a good vertical sensitivity in the lower-to-mid stratosphere (around 50 hPa), to monitor the relationship between the temperature decrease and the observed HNO₃ loss that occurs each year in the Antarctic stratosphere during the polar night. Since the HNO₃ depletion results from the formation of polar stratospheric clouds (PSCs) which trigger the development of the ozone (O₃) hole, its continuous monitoring is of high importance. We verify here, from the 10-year time evolution of HNO₃ together with temperature (taken from reanalysis at 50 hPa), the recurrence of specific regimes in the annual cycle of IASI HNO₃ and identify, for each year, the day and the 50 hPa temperature ("drop temperature") corresponding to the onset of strong HNO₃ depletion in the Antarctic winter. Although the measured HNO₃ total column does not allow the uptake of HNO₃ by different types of PSC particles along the vertical profile to be differentiated, an average drop temperature of 194.2 ± 3.8 K, close to the nitric acid trihydrate (NAT) existence threshold (~ 195 K at 50 hPa), is found in the region of potential vorticity lower than -10×10^{-5} K.m².kg⁻¹.s⁻¹ (similar to the 70° – 90° S equivalent latitude region during winter). The spatial distribution and inter-annual variability of the drop temperature are investigated and discussed. This paper highlights the capability of the IASI sounder to monitor the evolution of polar stratospheric HNO₃, a key player in the processes involved in the depletion of stratospheric O₃.

1 Introduction

The cold and isolated air masses found within the polar vortex during winter are associated with a strong denitrification of the stratosphere due to the formation of PSCs (composed of HNO₃, sulphuric acid (H₂SO₄) and water ice (H₂O)) (e.g. Peter, 1997; Voigt et al., 2000; von König, 2002; Schreiner et al., 2003; Peter and Groö, 2012). These clouds strongly affect the polar chemistry by (1) acting as surfaces for the heterogeneous activation of chlorine and bromine compounds, in turn leading to enhanced O₃ destruction (e.g. Solomon, 1999; Wang and Michelangeli, 2006; Harris et al., 2010; Wegner et al., 2012) and by (2) removing gas-phase HNO₃ temporarily or permanently through uptake by PSCs and sedimentation of large PSC particles to lower altitudes. The denitrification of the polar stratosphere during winter delays the reformation of ClONO₂, a chlorine reservoir, and, hence, intensifies the O₃ hole (e.g. Solomon, 1999; Harris et al., 2010; Tritscher et al., 2021). The heterogeneous reaction rates on PSC surfaces and the uptake of HNO₃ strongly depend on the temperature and on the PSC particle type. The

49 PSCs are classified into three different types based on their composition and optical properties: type Ia
50 solid nitric acid trihydrate - NAT ($\text{HNO}_3 \cdot (\text{H}_2\text{O})_3$), type Ib liquid supercooled ternary solution - STS
51 ($\text{HNO}_3/\text{H}_2\text{SO}_4/\text{H}_2\text{O}$ with variable composition) and type II, crystalline water-ice particles (likely
52 composed of a combination of different chemical phases) (e.g. Toon et al., 1986; Koop et al., 2000;
53 Voigt et al., 2000; Lowe and MacKenzie, 2008). In the stratosphere, they mostly consist of mixtures of
54 liquid/solid STS/NAT particles in varying number densities, with HNO_3 being the major constituent of
55 these particles. The large-size NAT particles of low number density are the principal cause of
56 sedimentation (Lambert et al., 2012; Pitts et al., 2013; Molleker et al., 2014; Lambert et al., 2016). The
57 formation temperature of STS (T_{STS}) and the thermodynamic equilibrium temperatures of NAT (T_{NAT})
58 and ice (T_{ice}) have been determined, respectively, as: ~ 192 K (Carslaw et al., 1995), ~ 195.7 K (Hanson
59 and Mauersberger, 1988) and ~ 188 K (Murphy and Koop, 2005) for typical 50 hPa atmospheric
60 conditions (5 ppmv H_2O and 10 ppbv HNO_3). While the NAT nucleation was thought to require pre-
61 existing ice nuclei, hence, temperatures below T_{ice} (e.g. Zondlo et al., 2000; Voigt et al., 2003), recent
62 observational and modelling studies have shown that HNO_3 starts to condense in early PSC season in
63 liquid NAT mixtures well above T_{ice} (~ 4 K below T_{NAT} , close to T_{STS}) even after a very short temperature
64 threshold exposure (TTE) to these temperatures but also slightly below T_{NAT} after a long TTE, whereas
65 the NAT existence persists up to T_{NAT} (Pitts et al., 2013; Hoyle et al., 2013; Lambert et al., 2016; Pitts
66 et al., 2018). It has been recently proposed that the higher temperature condensation results from
67 heterogeneous nucleation of NAT on meteoritic dust in liquid aerosol (Voigt et al., 2005; Hoyle et al.,
68 2013; Grooß et al., 2014; James et al., 2018; Tritscher et al., 2021). Further cooling below T_{STS} and T_{ice}
69 leads to nucleation of liquid STS, of solid NAT onto ice and of ice particles mainly from STS (type II
70 PSCs) (Lowe and MacKenzie, 2008). The formation of NAT and ice has also been shown to be triggered
71 by stratospheric mountain-waves (Carslaw et al., 1998; Hoffmann et al., 2017). Although the formation
72 mechanisms and composition of STS droplets in stratospheric conditions are well described (Toon et al.,
73 1986; Carslaw et al., 1995; Lowe and MacKenzie, 2008), the NAT and ice nucleation processes still
74 require further investigation (Tritscher et al., 2021). This could be important as the chemistry-climate
75 models (CCMs) generally oversimplify the heterogeneous nucleation schemes for PSC formation (Zhu
76 et al., 2015; Spang et al., 2018; Snels et al., 2019), preventing an accurate estimation of O_3 levels.

77
78 Over the last few decades, several satellite instruments have measured stratospheric HNO_3 (e.g.
79 MLS/UARS (Santee et al., 1999), MLS/Aura (Santee et al., 2007), MIPAS/ENVISAT (Piccolo and
80 Dudhia, 2007), ACE-FTS/SCISAT (Sheese et al., 2017) and SMR/Odin (Urban et al., 2009)).
81 Spaceborne instruments such as the CALIOP/CALIPSO lidar and MIPAS/Envisat measuring in the
82 infrared are capable of detecting and classifying PSC types, allowing their formation mechanisms to be
83 investigated (Lambert et al., 2016; Pitts et al., 2018; Spang et al., 2018, Tritscher et al., 2021 and
84 references therein); these satellite data complement in situ measurements (Voigt et al., 2005) and ground-
85 based lidar (Snels et al., 2019). From these available observational datasets, HNO_3 depletion has been
86 linked to PSC formation and detected below the T_{NAT} threshold (Santee et al., 1999; Urban et al., 2009;
87 Lambert et al., 2016; Ronsmans et al., 2018), but its relationship to PSCs still needs further investigation
88 given the complexity of the nucleation mechanisms that depend on several parameters (e.g. atmospheric
89 temperature, water and HNO_3 vapour pressure, time exposure to temperatures, temperature history).

90
91 In contrast to the limb satellite instruments mentioned above, the infrared nadir sounder IASI offers a
92 dense spatial sampling of the entire globe, twice a day (Section 2). While it cannot provide a vertical
93 profile of HNO_3 similar to that from the limb sounders, IASI provides reliable total column
94 measurements of HNO_3 characterized by a maximum sensitivity in the low-middle stratosphere around
95 50 hPa (20 km) during the dark Antarctic winter (Ronsmans et al., 2016, 2018) where PSCs form (Voigt
96 et al., 2005; Lambert et al., 2012; Spang et al., 2016, 2018). This study aims to explore the 10-year
97 continuous HNO_3 measurements from IASI to provide a long-term global picture of depletion and of its

98 dependence on temperatures during polar winter (Section 3). The temperature corresponding to the onset
99 of the strong depletion in HNO₃ records (here referred to as ‘drop temperature’) is identified in Section
100 4 for each observed year and discussed in the context of previous studies.

101 102 **2 Data**

103
104 The HNO₃ data used in the present study are obtained from measurements of the Infrared Atmospheric
105 Sounding Interferometer (IASI) onboard the Metop-A satellite. IASI measures the Earth’s and
106 atmosphere’s radiation in the thermal infrared spectral range (645 - 2760 cm⁻¹), with a 0.5 cm⁻¹ apodized
107 resolution and a low radiometric noise (Clerbaux et al., 2009; Hilton et al., 2012). Thanks to its polar
108 sun-synchronous orbit with more than 14 orbits a day and a field of view of four simultaneous footprints
109 of 12 km at nadir, IASI provides global coverage twice a day (9.30 AM and PM mean local solar time).
110 That extensive spatial and temporal sampling in the polar regions is key to this study.

111
112 The HNO₃ vertical profiles are retrieved on a uniform vertical 1 km grid of 41 layers (from the surface
113 to 40 km with an extra layer above to 60 km) in near-real-time by the Fast Optimal Retrieval on Layers
114 for IASI (FORLI) software, using the optimal estimation method (Rodgers, 2000). Detailed information
115 on the FORLI algorithm and retrieval parameters specific to HNO₃ can be found in previous papers
116 (Hurtmans et al., 2012; Ronsmans et al., 2016). For this study, only the total columns (v20151001) are
117 used, considering (1) the low vertical resolution of IASI with only one independent piece of information
118 (full width at half maximum - FWHM - of the averaging kernels of ~30 km), (2) the limited sensitivity
119 of IASI to tropospheric HNO₃, (3) the dominant contribution of the stratosphere to the HNO₃ total
120 column and (4) the largest sensitivity of IASI in the region of interest, i.e. in the low and mid-stratosphere
121 (from ~70 to ~30 hPa), where the HNO₃ abundance is the highest (Ronsmans et al., 2016). The IASI
122 measurements capture the expected depletion of HNO₃ within the polar night, as illustrated in Fig. 1 that
123 shows examples of vertical HNO₃ profiles retrieved within the dark Antarctic vortex (above Arrival
124 Heights) and outside the vortex (above Lauder). The retrieved profiles are shown along with their
125 associated total retrieval error and averaging kernels (the total column averaging kernel and the so-called
126 “sensitivity profile” are also represented; see Ronsmans et al., 2016 for more details). The total column
127 averaging kernel (in black) indicates the sensitivity of the total column measurement to changes in the
128 vertical distribution of HNO₃, hence, the altitude to which the retrieved total column is mainly
129 sensitive/representative, while the sensitivity profile indicates the extent to which the retrieval at one
130 specific altitude comes from the spectral measurement rather than the a priori. Above Arrival Heights
131 during the dark Antarctic winter, we clearly see depleted HNO₃ levels in the low and mid-stratosphere
132 and the altitude of maximum sensitivity at around 30 hPa for this case (values of ~1 along the total
133 column averaging kernel around that level). In contrast, at Lauder, HNO₃ levels larger than the a priori
134 are observed in the stratosphere with a larger range of maximum sensitivity. The total columns are
135 associated with a total retrieval error ranging from around 3% at mid- and polar latitudes (except above
136 Antarctica) to 25% above cold Antarctic surface during winter and with a low absolute bias smaller than
137 12% when compared to ground-based FTIR measurements, in polar regions over the altitude range
138 where the IASI sensitivity is the largest (see Hurtmans et al., 2012 and Ronsmans et al., 2016 for more
139 details). The highest retrieval error measured over the Antarctic arises from a weaker sensitivity above
140 very cold surface with a degrees of freedom for signal (DOFS) of 0.95, as well as ~~and~~ from a poor
141 knowledge of the seasonally and wavenumber-dependent emissivity above ice surfaces, ~~which induces~~
142 larger forward model errors. In order to expand on the comparisons against FTIR measurements, which
143 cannot be made during the polar night, Fig. 2 (top panel) presents the time series of daily IASI total
144 HNO₃ columns co-located with MLS measurements within 2.5°x2.5° grid boxes, averaged in the 70°S–
145 90°S equivalent latitude band. In order to account for the vertical sensitivity of IASI, the averaging
146 kernels associated with each co-located IASI retrieved profile were applied to the MLS profiles for this

147 cross-comparison. The MLS mixing ratio profiles over the 215-1.5 hPa pressure range were first
148 interpolated to the FORLI pressure grids and extended down to the surface by using the FORLI-HNO₃
149 a priori profile, and then converted into partial columns. Similar variations in the HNO₃ column are
150 captured by the two instruments, with an excellent agreement in particular for the timing of the strong
151 HNO₃ depletion within the inner vortex core. Note that a similar good agreement between the two
152 satellite datasets is obtained in other latitude bands (see Fig. 2 bottom panel for the 50°S–70°S equivalent
153 latitude band; the other bands are not shown).

154
155 Quality flags similar to those developed for O₃ in previous IASI studies (Wespes et al., 2017) were
156 applied a posteriori to exclude data (i) with a corresponding poor spectral fit (e.g. based on quality flags
157 rejecting biased or sloped residuals, fits with maximum number of iterations exceeded), (ii) with less
158 reliability (e.g. based on quality flags rejecting suspect averaging kernels, data with less sensitivity
159 characterized by a DOFS lower than 0.9) or (iii) with tropospheric cloud contamination (defined by a
160 fractional cloud cover ≥ 25 %). Note that the HNO₃ total column distributions illustrated in sections
161 below use the median as a statistical average since it is more robust against the outliers than the mean.

162
163 Temperature and potential vorticity (PV) fields are taken from the ECMWF ERA Interim Reanalysis
164 dataset, respectively at 50 hPa and at the potential temperature of 530 K (corresponding to ~ 20 km
165 altitude where the IASI sensitivity to HNO₃ is the highest during the Southern Hemisphere (S.H.) winter
166 (Ronsmans et al., 2016)). Because the HNO₃ uptake by PSCs starts within a few degrees below T_{NAT}
167 (~ 195.7 K at 50 hPa (Hanson and Mauersberger, 1988)) depending on the meteorological conditions
168 (Pitts et al., 2013; Hoyle et al., 2013; Lambert et al., 2016; Pitts et al., 2018), a threshold temperature of
169 195 K is considered in the sections below to identify regions of potential PSC existence. The potential
170 vorticity is used to delimit dynamically consistent areas in the polar regions. In what follows, we use
171 either the equivalent latitudes ("eqlat", calculated from PV fields at 530 K) or the PV values to
172 characterize the relationship between HNO₃ and temperatures in the cold polar regions. Uncertainties in
173 ERA-Interim temperatures will also be discussed below.

174 175 **3 Annual cycle of HNO₃ vs temperatures**

176
177 Figure 3a shows the yearly HNO₃ cycle (solid lines, left axis) in the southernmost equivalent latitudes
178 (70° - 90° S) as measured by IASI over the whole study period (2008–2017). The total HNO₃ variability
179 in such equivalent latitudes has already been discussed in a previous IASI study (Ronsmans et al., 2018),
180 where the contribution of the PSCs to the HNO₃ variations was highlighted. The temperature time series,
181 taken at 50 hPa, is represented as well (dashed lines, right axis). From this figure, different regimes of
182 HNO₃ total columns vs temperature can be observed throughout the year and from one year to another.
183 In particular, we define here three main regimes (R1, R2 and R3) during the HNO₃/temperature annual
184 cycle. The full cycle and the main regimes in the 70° - 90° S eqlat region are further represented in Fig.
185 3b that shows a histogram of the HNO₃ total columns as a function of temperature for the year 2011.
186 Similar histograms are observed for the other years in the 10-year study period (not shown). The orange
187 horizontal and vertical lines in Fig. 3a and Fig. 3b, respectively, represent the 195 K threshold
188 temperature used to identify the onset of HNO₃ uptake by PSCs (see Section 2). The three regimes
189 identified are:

- 190
191 - R1 is defined by the maxima in the total HNO₃ abundances covering the months of April and
192 May ($\sim 3 \times 10^{16}$ molec.cm⁻²), when the 50 hPa temperature strongly decreases (from ~ 220 to ~ 195
193 K). These high HNO₃ levels result from low sunlight, preventing photodissociation, along with
194 the heterogeneous hydrolysis of N₂O₅ to HNO₃ during autumn before the formation of polar
195 stratospheric clouds (Keys et al., 1993; Santee et al., 1999; Urban et al., 2009; de Zafra and

196 Smyshlyaev, 2001). This period also corresponds to the onset of the development of the southern
 197 polar vortex, which is characterized by strong diabatic descent with weak latitudinal mixing
 198 across its boundary, isolating polar HNO₃-rich air from lower-latitude airmasses. The end of the
 199 R1 period marks the start of the strong total HNO₃ decrease that intensifies later in R2.
 200
 201 - R2, which extends from June to October, follows the onset of the strong decrease in HNO₃ total
 202 columns that starts around mid-May in most years when the temperatures fall below 195 K. After
 203 a steep initial decline in total HNO₃, R2 is characterized by a plateau of total HNO₃ minima. For
 204 much of this regime, average HNO₃ total columns are below 2×10^{16} molec.cm⁻² and the 50 hPa
 205 temperatures range mostly between 180 and 190 K.
 206
 207 - R3 starts in October when sunlight returns and the 50 hPa temperatures rise above 195 K. Despite
 208 50 hPa temperatures increasing up to 240 K in summer, the HNO₃ total columns stagnate at the
 209 R2 plateau levels (around 1.5×10^{16} molec.cm⁻²). This regime likely reflects the photolysis of NO₃
 210 and HNO₃ itself (Ronsmans et al., 2018) as well as the permanent denitrification of the mid-
 211 stratosphere, caused by sedimentation of PSCs. The likely renitrification of the lowermost
 212 stratosphere (e.g. Braun et al., 2019; Lambert et al., 2012), where the HNO₃ concentrations and
 213 the IASI sensitivity to HNO₃ are lower (Ronsmans et al., 2016), cannot be inferred from the IASI
 214 total column measurements. The plateau lasts until approximately February, when HNO₃ total
 215 column slowly starts increasing, reaching the April-May maximum in R1.
 216

217 As illustrated in Fig. 3a, the three regimes are observed each year with, however, some interannual
 218 variations. For instance, the sudden stratospheric warming (SSW) that occurred in 2010 (see the
 219 temperature time series at 20 hPa for the year 2010; green dotted line) yielded higher HNO₃ total columns
 220 (see green solid line in July - September) (de Laat and van Weele, 2011; Klekociuk et al., 2011; WMO,
 221 2014; Ronsmans et al., 2018).
 222

223 Figure 3c shows the evolution of the relationship between the daily averaged HNO₃ (calculated from a
 224 7-day moving average) with the highest occurrence (in bins of 0.1×10^{16} molec.cm⁻² and of 2K) and the
 225 50 hPa temperature, over the 10-year study period. The ~~red-orange~~ vertical line represents the 195 K
 226 threshold temperature. Figure 3c also highlights ~~the~~ large interannual variability in total HNO₃ in R3,
 227 while the strong depletion in HNO₃ in R2 is consistent every year. Given that PSC formation spans a
 228 large range of altitudes (typically between 10 and 30 km) (Höpfner et al., 2006, 2009; Spang et al., 2018;
 229 Pitts et al., 2018) and that IASI has maximum sensitivity to HNO₃ around 50 hPa (Hurtmans et al., 2012;
 230 Ronsmans et al., 2016), the temperatures at two other pressure levels, namely 70 and 30 hPa (i.e. ~15
 231 and ~25 km), have also been tested to investigate the relationship between HNO₃ and temperature in the
 232 low and mid-stratosphere. The results (not shown here) exhibit a similar HNO₃-temperature behavior at
 233 the different levels with, as expected, lower and higher temperatures in R2, respectively, at 30 hPa and
 234 at 70 hPa (temperatures down to ~180 K at 30 hPa and down to ~185 K at 70 hPa, as compared to
 235 temperatures down to ~182 K at 50 hPa, are observed), but still below the NAT formation threshold at
 236 these pressure levels ($T_{NAT} \sim 193$ K at 30 hPa and ~197 K at 70 hPa) (Lambert et al., 2016). Therefore,
 237 the altitude range of maximum IASI sensitivity to HNO₃ (see Section 2) is characterized by temperatures
 238 that are below the NAT formation threshold at these pressure levels, enabling PSC formation and the
 239 denitrification process. Furthermore, the consistency between the 195 K threshold temperature taken at
 240 50 hPa and the onset of the strong total HNO₃ depletion seen in IASI data (see Fig. 3a) is in agreement
 241 with the largest NAT area that starts to develop in June around 20 km (Spang et al., 2018), which justifies
 242 the use of the 195 K temperature at that single representative level in this study.
 243

244 4 Onset of HNO₃ depletion and drop temperature detection

245
246
247
248
249
250
251
252
253
254
255
256
257
258
259
260
261
262
263
264
265
266
267
268
269
270
271
272
273
274
275
276
277
278
279
280
281
282
283
284
285
286
287
288
289
290
291
292
293

To identify the spatial and temporal variability of the onset of the depletion phase, the daily time evolution of HNO₃ during the first 10 years of IASI measurements and the temperatures at 50 hPa are explored. In particular, the second derivative of HNO₃ total column with respect to time is calculated to detect the strongest rate of decrease seen in the HNO₃ time series and to identify its associated day and 50 hPa temperature.

4.1 HNO₃ vs temperature time series

Figure 4 shows the time series of the second derivative of HNO₃ total column ~~with respect to time~~ (blue) and of the temperature (red) with respect to time, averaged in the area of potential vorticity smaller than $-10 \times 10^{-5} \text{ K.m}^2.\text{kg}^{-1}.\text{s}^{-1}$ at the potential temperature of 530 K to encompass the region inside the inner polar vortex where the temperatures are the coldest and the largest depletion of total HNO₃ occurs (Ronsmans et al., 2018). The use of that PV threshold value explains the gaps in the time series during the summer when the PV does not reach such low levels, while the time series averaged in the 70°- 90° S eq-lat band (dashed blue for the second derivative of HNO₃ and grey for the temperature) covers the full year. Note that the HNO₃ time series has been smoothed with a simple spline data interpolation function to avoid gaps in order to calculate the second derivative of HNO₃ total column with respect to time as the daily second-difference in HNO₃ total columns. The horizontal red line shows the 195 K threshold.

As already illustrated in Fig. 3a and Fig. 3c, the strongest rate of HNO₃ depletion (i.e. the second derivative minimum) is found closely around the time that temperatures drop below the 195 K threshold ~~(at exactly or a few days after the detection of the 195 K threshold temperature, particularly (except~~ for the year 2009 that shows a longest delay), within a few days to a few weeks (4 to 23 days) after total HNO₃ reaches its maximum, i.e. between the 11th of May (2013) and the 8th of June (2009). The 50 hPa drop temperatures, i.e. the temperature associated with the strongest rate of HNO₃ depletion detected from IASI, are between 189.2 K and 198.6 K, with the exception of the year 2014, which shows a drop temperature of 202.8 K. On average over the 10 years of studied IASI measurements, a 50 hPa drop temperature of $194.2 \text{ K} \pm 3.8 \text{ K}$ (1σ standard deviation) is found. Knowing that T_{NAT} can be higher or lower depending on the atmospheric conditions and that NAT starts to nucleate from $\sim 2-4 \text{ K}$ below T_{NAT} (Pitts et al., 2011; Hoyle et al., 2013; Lambert et al., 2016), the results here tend to demonstrate the consistency between the 50 hPa drop temperature and the PSC existence temperature in that altitude region. Note that the range observed in the 50 hPa drop temperature could reflect variations in the preponderance of one type of PSCs over another from one year to the next. The results further justify the use of the single 50 hPa level for characterizing and investigating the onset of HNO₃ depletion from IASI. Nevertheless, given the range of maximum IASI sensitivity to HNO₃ around 50 hPa, typically between 70 and 30 hPa (Ronsmans et al., 2016), the drop temperatures are also calculated at these two other pressure levels (not shown here) in order to estimate the uncertainty of the calculated drop temperature defined in this study at 50 hPa. The 30 hPa and 70 hPa drop temperatures range respectively over $185.7 \text{ K} - 194.9 \text{ K}$ and over $194.8 \text{ K} - 203.7 \text{ K}$, with an average of $192.0 \pm 2.9 \text{ K}$ and $198.0 \pm 3.2 \text{ K}$ (1σ standard deviation) over the ten years of IASI. The average values at 30 hPa and 70 hPa fall within the 1σ standard deviation associated with the average drop temperature at 50 hPa. It is also worth noting the agreement between the drop temperatures and the NAT formation threshold at these two pressure levels ($T_{NAT} \sim 193 \text{ K}$ at 30 hPa and $\sim 197 \text{ K}$ at 70 hPa) (Lambert et al., 2016). Finally, it should be noted that, because the size, shape or location of the vortex vary slightly over the altitude range to which IASI is sensitive (from ~ 30 to ~ 70 hPa during the polar night), the use of a single potential temperature surface for the calculation of drop temperatures could introduce some uncertainties into the results. However, several tests suggest that these variations of the vortex are overall minor and, hence, have only limited

294 influence on the identification of the inner polar vortex (delimited by a PV value of $-10 \times 10^{-5} \text{K.m}^2.\text{kg}^{-1}.\text{s}^{-1}$ at 530 K) and on the determination of the average drop temperature inside that region.
295
296

297 Figures 5a and b show the climatological zonal distribution of HNO_3 total columns and of the
298 temperature at 50 hPa, respectively, spanning the $55^\circ \text{S} - 90^\circ \text{S}$ geographic latitude band over the first
299 ten years of IASI, with, superimposed, three isocontour levels of potential vorticity (-10 , -8 and -5×10^{-5}
300 $\text{K.m}^2.\text{kg}^{-1}.\text{s}^{-1}$ in blue, cyan and black, respectively) and the isocontours for the 195 K temperature (pink)
301 and for the averaged 194.2 K drop temperature (purple) at 50 hPa. They further illustrate the relationship
302 between the IASI total HNO_3 columns and the 50 hPa temperatures. The climatological (2008-2017) PV
303 isocontour of $-10 \times 10^{-5} \text{K.m}^2.\text{kg}^{-1}.\text{s}^{-1}$ is clearly shown to separate well the region of strong depletion in
304 total HNO_3 , according to the latitude and the time, until October. The red vertical dashed line indicates
305 the ~~annual~~ average of the dates on which the 50 hPa drop temperatures are calculated in the area of $\text{PV} \leq$
306 $-10 \times 10^{-5} \text{K.m}^2.\text{kg}^{-1}.\text{s}^{-1}$ ($194.2 \pm 3.8 \text{K}$; see Fig. 4) over the first ten years of IASI. It shows that the
307 strongest rate of HNO_3 depletion occurs on average at the end of May (24 May), a few days after the
308 temperature decreases below 195 K. The yearly zonally averaged time series over the 10-year study
309 period can be found in Fig. 6, which shows that IASI measures similar HNO_3 total column zonal
310 distributions every year, in particular with respect to the edge of the collar region and of the region of
311 strong depletion (respectively delimited by the PV isocontours of $-5 \times 10^{-5} \text{K.m}^2.\text{kg}^{-1}.\text{s}^{-1}$ and of -10×10^{-5}
312 $\text{K.m}^2.\text{kg}^{-1}.\text{s}^{-1}$ at 530 K). ~~Like for Fig.4, A~~ an exact timing or a ~~delay of a~~ few days between the ~~time that~~
313 ~~temperatures drop below the 195 K threshold~~ ~~detection of the averaged 195 K threshold temperature~~ and
314 the start of the HNO_3 depletion is visible every year in Fig. 6. ~~A longest delay is also observed in~~
315 ~~particular, for~~ the year 2009 ~~shows the longest delay (see also Fig. 4)~~. Note that the mismatch ~~observed~~
316 ~~inbetween~~ the 10-year average ~~between the detection of the averaged of the dates on which the~~ 195 K
317 threshold temperature ~~is reached~~ and ~~the averagethat of the~~ dates for the drop temperatures (see Fig. 5 a
318 and b) is driven by the year 2013, which is characterized by the lowest temperatures during the Antarctic
319 winter over the 10-year study period and, hence, the earliest date for the drop temperature (11th of May;
320 see Fig. 4 and Fig. 6).

322 4.2 Spatial distribution of drop temperatures

323
324 To explore the capability of IASI to monitor the onset of HNO_3 depletion at a large scale, figure 7 shows,
325 for each year of the study period, the spatial distribution of the 50 hPa drop temperatures based on the
326 second derivative minima of total HNO_3 averaged in $1^\circ \times 1^\circ$ grid cells. The region of interest here is
327 delimited by a PV value of $-8 \times 10^{-5} \text{K.m}^2.\text{kg}^{-1}.\text{s}^{-1}$ at 530 K, in order to investigate an area a bit larger
328 than the inner vortex core that was the focus of the preceding discussion (delineated in green in figure 7
329 by the PV isocontour of $-10 \times 10^{-5} \text{K.m}^2.\text{kg}^{-1}.\text{s}^{-1}$ averaged over the interval 10 May to 15 July). The
330 isocontour of $-10 \times 10^{-5} \text{K.m}^2.\text{kg}^{-1}.\text{s}^{-1}$ for the minimum PV (in cyan) encountered at 530 K over the 10
331 May to 15 July period for each year, as well as the isocontours of 195 K for the average temperatures
332 and the minimum temperatures, are also represented. The calculated drop temperatures corresponding
333 to the onset of HNO_3 depletion inside the averaged PV isocontour are found to vary between ~ 180 and
334 $\sim 210 \text{K}$ and the corresponding dates range between \sim mid-May and mid-July (not shown here). Although
335 the range of drop temperatures and dates for $1^\circ \times 1^\circ$ bins is broader than that found for the inner vortex
336 averages discussed above, the results are qualitatively consistent. For example, the year 2014 that shows
337 the highest inner vortex average drop temperature in Figure 4 is characterized by the highest drop
338 temperatures above the eastern Antarctic. Note, however, that the high extremes in the drop temperature,
339 mainly found above the eastern Antarctic, should be considered with caution: they correspond to specific
340 regions above ice surfaces with emissivity features that are known to yield errors in the IASI retrievals
341 (Hurtmans et al., 2012; Ronsmans et al., 2016). Indeed, bright land surfaces such as ice might in some
342 cases lead to poor HNO_3 retrievals. Although wavenumber-dependent surface emissivity atlases are used

343 in FORLI (Hurtmans et al., 2012), this parameter remains critical and causes poorer retrievals that, in
344 some instances, pass through the series of quality filters and could affect the drop temperature
345 calculation.

346
347 The averaged isocontour of 195 K encircles fairly well the area of HNO₃ drop temperatures lower than
348 195 K (typically from ~187 K to ~195 K), which means that the bins inside that area include airmasses
349 that experience the NAT threshold temperature during a long time over the 10 May – 15 July period.
350 That area encompasses the inner vortex core (delimited by the isocontour of $-10 \times 10^{-5} \text{ K.m}^2.\text{kg}^{-1}.\text{s}^{-1}$ for
351 the PV averaged over the 10 May – 15 July period) and shows pronounced minima (lower than -0.5×10^{14}
352 molec.cm⁻².d⁻²) in the second derivative of the HNO₃ total column with respect to time (not shown here),
353 which indicate a strong and rapid HNO₃ depletion. The area enclosed between the two isocontours of
354 195 K for the temperatures, the averaged one and the one for the minimum temperatures, shows generally
355 higher drop temperatures and weakest minima (larger than -0.5×10^{14} molec.cm⁻².d⁻²) in the second
356 derivative of the HNO₃ total column (not shown). That area is also typically enclosed by the isocontour
357 of $-10 \times 10^{-5} \text{ K.m}^2.\text{kg}^{-1}.\text{s}^{-1}$ for the minimum PV, meaning that the bins inside correspond, at least for one
358 day over the 10 May – 15 July period, to airmasses located at the inner edge of the vortex and
359 characterized by temperature lower than the NAT threshold temperature. The fact that the weakest
360 minima in the second derivative of total HNO₃ are observed in that area (not shown) indicates a weak
361 and slow HNO₃ depletion that might be explained by air masses at the inner edge of the vortex
362 experiencing only a short period with temperatures below the NAT threshold temperature. It could also
363 reflect mixing with strongly HNO₃-depleted and colder airmasses from the inner vortex core. Mixing
364 with these already depleted airmasses could also explain the higher drop temperatures detected in those
365 bins. These sometimes unrealistic high drop temperatures are generally detected later (after the strong
366 HNO₃ depletion occurs in the inner vortex core, i.e. after the 10 May – 15 July period considered here –
367 not shown), which supports the transport, in those bins, of previously HNO₃-depleted airmasses and the
368 likely mixing at the edge of the vortex. Note, however, that previous studies have shown a generally
369 weak mixing in the Antarctic between the edge region and the vortex core (e.g. Roscoe et al., 2012).
370 Finally, these spatial variations might also partly reflect some uncertainty in the drop temperature
371 calculation, introduced by the use of temperature at a single pressure level (50 hPa) and of PV on a single
372 potential temperature surface (530 K) while the sensitivity of IASI to changes in the HNO₃ profiles
373 extends over a range from ~30 to ~70 hPa during the polar night. It should be noted that biases in the
374 ECMWF ERA Interim temperatures used in this work are too small to explain the large range of drop
375 temperatures calculated here. Indeed, Lambert and Santee (2018) found only a small warm bias, with
376 median differences around 0.5 K, reaching 0–0.25 K in the southernmost regions of the globe at ~68–21
377 hPa where PSCs form, through comparisons with the Constellation Observing System for Meteorology,
378 Ionosphere and Climate (COSMIC) data.

379
380 Except above some parts of Antarctica which are prone to larger retrieval errors and where unrealistic
381 high drop temperatures are found, the overall range in the 50 hPa drop temperature for total HNO₃ inside
382 the isocontour for the averaged temperature of 195 K typically extends from ~187 K to ~195 K, which
383 falls within the range of PSC nucleation temperature at 50 hPa: from slightly below T_{NAT} to around 3-4
384 K below the ice frost point - T_{ice} - depending on atmospheric conditions, on TTE and on the specific
385 formation mechanism (i.e., the type of PSC developing) (Pitts et al., 2011; Peter and Grooß, 2012; Hoyle
386 et al., 2013). This underlines well the benefit of the excellent spatial and temporal coverage of IASI,
387 which allows the rapid and critical depletion phase to be captured in detail over a large scale.

388
389 **5 Conclusions**

390

391 In this paper, we have explored the added value of the dense HNO₃ total column dataset provided by the
392 IASI/Metop-A satellite over a full decade (2008–2017) for monitoring the stratospheric depletion phase
393 that occurs each year in the S.H. and for investigating its relationship to the NAT formation temperature.
394 To that end, we focused on and delimited the coldest polar region of the S.H. using a specific PV value
395 at 530 K (~50 hPa, PV of $-10 \times 10^{-5} \text{ K.m}^2.\text{kg}^{-1}.\text{s}^{-1}$) and stratospheric temperatures at 50 hPa, taken from
396 the ECMWF ERA Interim reanalysis. That single representative pressure level has been considered in
397 this study given the maximum sensitivity of IASI to HNO₃ around that level, which lies in the range
398 where the PSCs formation/denitrification processes occur.

400 The annual cycle of total HNO₃, as observed from IASI, has first been characterized according to the
401 temperature evolution. Three regimes (R1 to R3) in the total HNO₃ - 50 hPa temperature relationship
402 were highlighted from the time series over the S.H. polar region: R1 is defined during April and May
403 and characterized by a rapid decrease in 50 hPa temperatures while HNO₃ accumulates over the pole;
404 R2, from June to October, follows the onset of the depletion that starts around mid-May in most years
405 when the 50 hPa temperatures fall below 195 K (considered here as the onset of PSC nucleation phase
406 at that level), with a strong consistency from year to year; R3, defined from October through March
407 when total HNO₃ remains at low R2 plateau levels, despite the return of sunlight and heat, characterizes
408 the strong denitrification of the stratosphere, likely due to PSC sedimentation to lower levels where the
409 IASI sensitivity is low. For each year over the 10-year study period, the use of the second derivative of
410 the HNO₃ column versus time was then found to be particularly valuable to detect the onset of the HNO₃
411 condensation into PSCs. It is captured, on average from IASI, a few days before June with a delay of 4–
412 23 days after the maximum in total HNO₃. The corresponding temperatures ('drop temperatures') were
413 detected between 189.2 K and 202.8 K ($194.2 \pm 3.8 \text{ K}$ on average over the 10 years), which tends to
414 demonstrate the good consistency between the 50 hPa drop temperature and the PSC formation
415 temperatures in that altitude region. Finally, the annual and spatial variability (within $1^\circ \times 1^\circ$) in the drop
416 temperature was further explored from IASI total HNO₃. Inside the isocontours of 195 K for the average
417 temperatures and of $-10 \times 10^{-5} \text{ K.m}^2.\text{kg}^{-1}.\text{s}^{-1}$ for the averaged PV at 530 K, the drop temperatures are
418 detected between ~mid-May and mid-July, typically range between ~187 K to ~195 K and are associated
419 with the lowest minima (lower than $-0.5 \times 10^{14} \text{ molec.cm}^{-2}.\text{d}^{-2}$) in the second derivative of the HNO₃ total
420 column with respect to time, indicating a strong and rapid HNO₃ depletion. Except for unrealistic drop
421 temperatures (~210 K) that were found in some years above eastern Antarctica and suspected to result
422 from unfiltered poor quality retrievals arising from emissivity issues above ice, the range of drop
423 temperatures is interestingly found to be in line with the PSC nucleation temperature that is known, from
424 previous studies, to strongly depend on several factors (e.g. meteorological conditions, HNO₃ vapour
425 pressure, temperature threshold exposure, presence of meteoritic dust). At the edge of the vortex,
426 considering the isocontours of 195 K for the minimum temperatures or of $-10 \times 10^{-5} \text{ K.m}^2.\text{kg}^{-1}.\text{s}^{-1}$ for the
427 minimum PV, higher and later drop temperatures along with weakest minima in the second derivative
428 of the HNO₃ total column with respect to time, indicating a slow HNO₃ depletion, are found. These
429 likely result from a short temperature threshold exposure or mixing with already depleted airmasses from
430 the inner vortex core. The results of this study highlight the ability of IASI to measure the variations in
431 total HNO₃ and, in particular, to capture and monitor the rapid depletion phase over the whole Antarctic
432 region.

434 We show in this study that the IASI dataset allows the variability of stratospheric HNO₃ throughout the
435 year (including the polar night) in the Antarctic to be captured. In that respect, it offers observational
436 means to monitor the relation of HNO₃ to temperature and the related formation of PSCs. Despite the
437 limited vertical resolution of IASI which does not allow investigation of the HNO₃ uptake by the
438 different types of PSCs during their formation and growth along the vertical profile, the HNO₃ total
439 column measurements from IASI constitute an important new dataset for exploring the strong polar

440 depletion over the whole stratosphere. This is particularly relevant considering the mission continuity,
441 which will span several decades with the planned follow-on missions. Indeed, thanks to the three
442 successive instruments (IASI-A launched in 2006 and still operating, IASI-B in 2012, and IASI-C in
443 2018) that demonstrate an excellent stability of the Level-1 radiances, the measurements will soon
444 provide an unprecedented long-term dataset of HNO₃ total columns. Further work could also make use
445 of this unique data set to investigate the relation between HNO₃, O₃, and meteorology in the changing
446 climate.

447
448

449 **Data availability**

450 The IASI HNO₃ data processed with FORLI-HNO₃ v0151001 are available upon request to the
451 corresponding author.

452

453 **Author contributions**

454 C.W. and G.R. performed the analysis, wrote the manuscript and prepared the figures. L.C. contributed
455 to the analysis. S.S., P.-F. C. and L.C. contributed to the interpretation of the results. D.H. was
456 responsible for the retrieval algorithm development and the processing of the IASI HNO₃ dataset. All
457 authors contributed to the writing of the text and reviewed the manuscript.

458

459 **Competing interests**

460 The authors declare no competing interests.

461

462 **Acknowledgements**

463 IASI has been developed and built under the responsibility of the Centre National d'Etudes Spatiales
464 (CNES, France). It is flown on board the Metop satellites as part of the EUMETSAT Polar System. The
465 IASI L1 data are received through the EUMETCast near-real-time data distribution service. The research
466 was funded by the F.R.S.-FNRS, the Belgian State Federal Office for Scientific, Technical and Cultural
467 Affairs (Prodex arrangement 4000111403 IASI.FLOW) and EUMETSAT through the Satellite
468 Application Facility on Atmospheric Composition Monitoring (ACSAF). G. Ronsmans is grateful to the
469 Fonds pour la Formation à la Recherche dans l'Industrie et dans l'Agriculture of Belgium for a PhD
470 grant (Boursier FRIA). L. Clarisse is a research associate supported by the F.R.S.-FNRS. C. Clerbaux is
471 grateful to CNES for financial support. S. Solomon is supported by the National Science Foundation
472 (NSF-1539972). We also would like to thank the three reviewers for their helpful comments and
473 corrections and, in particular, M. Santee for her in-depth reviews, which have substantially improved
474 the paper quality.

475

476

477

478

479

480

481

482

483

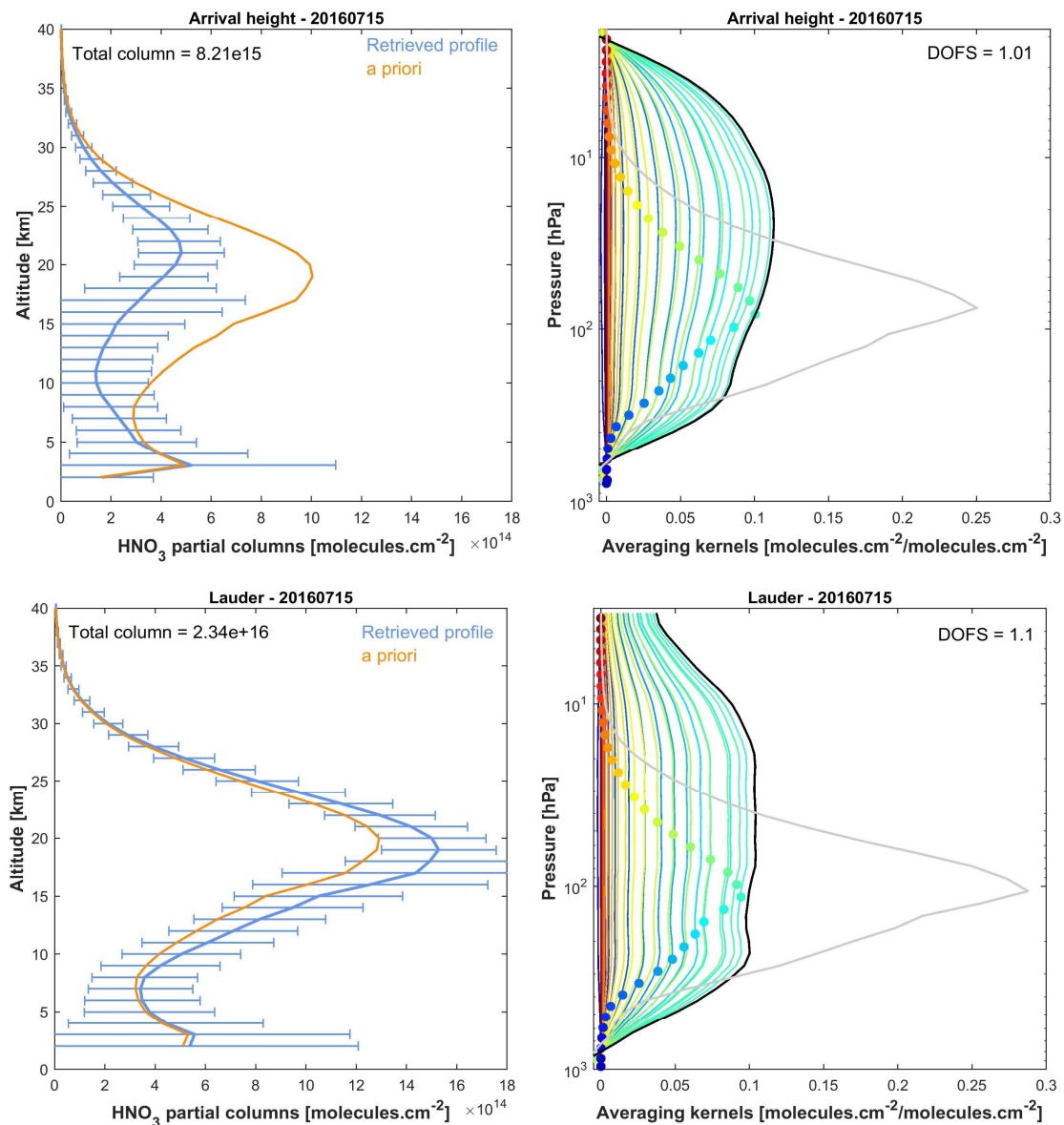
484

485

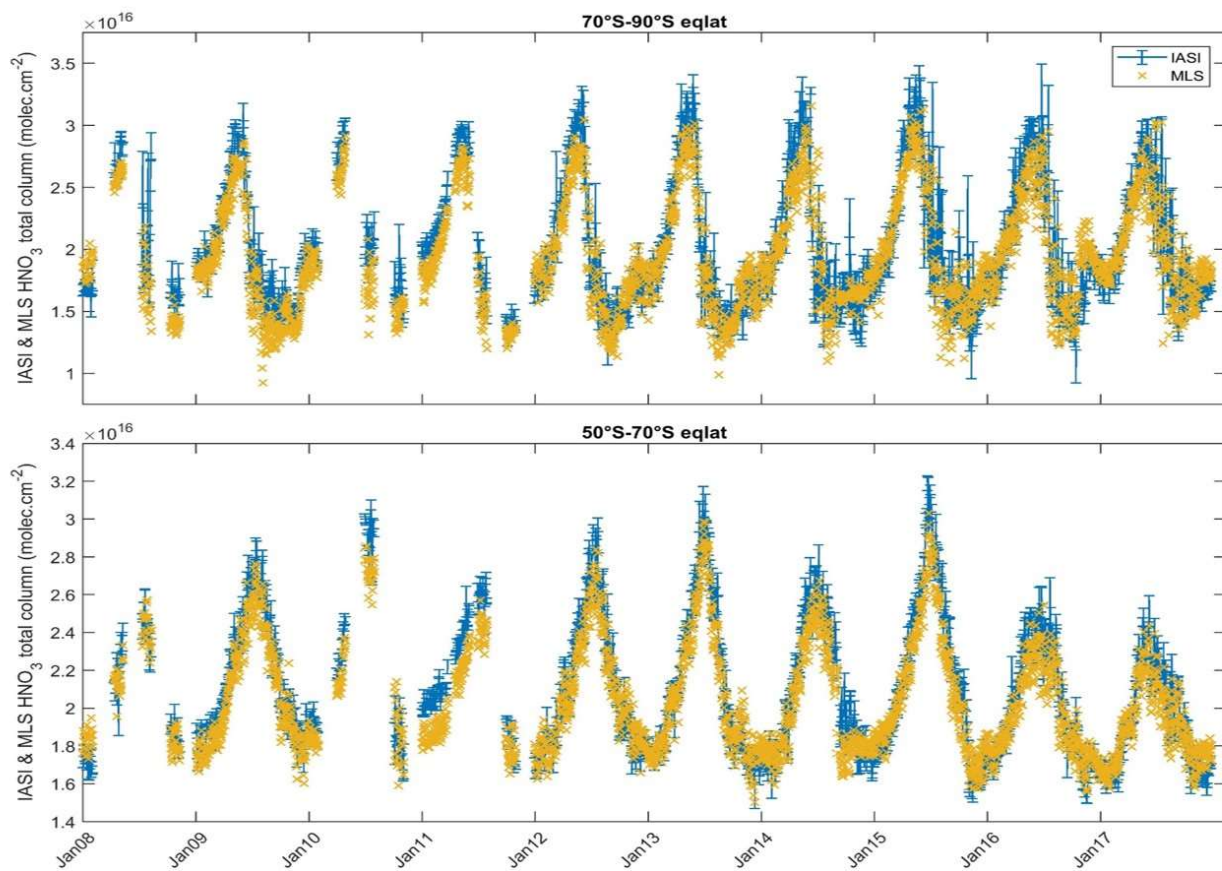
486

487

488

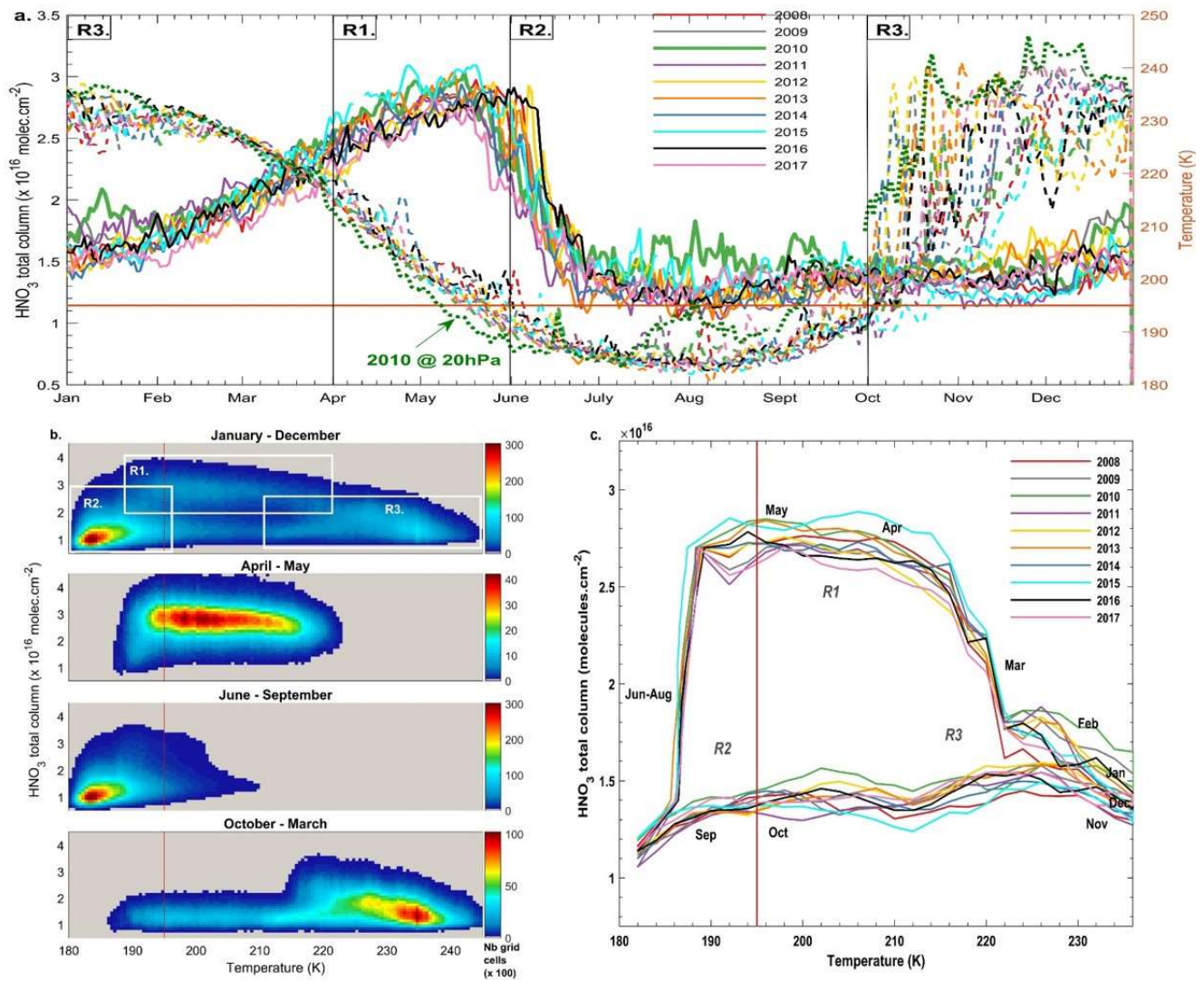
492
493

494 Figure 1. Examples of IASI HNO₃ vertical profiles (in molec.cm⁻²) with corresponding averaging kernels (in
 495 molec.cm⁻²/molec.cm⁻²; colored lines, with the altitude of each kernel represented by the colored dots)
 496 along with the total column averaging kernels (black) and the sensitivity profiles (grey) (both divided by 10) above
 497 Arrival Heights (77.49°S, 166.39°E, top panels) and Lauder (45.03°S, 169.40°E; bottom panels). The error bars
 498 associated with the HNO₃ vertical profile represent the total retrieval error. The a priori profile is also represented.
 499 The total column and the DOFS values are indicated.
 500



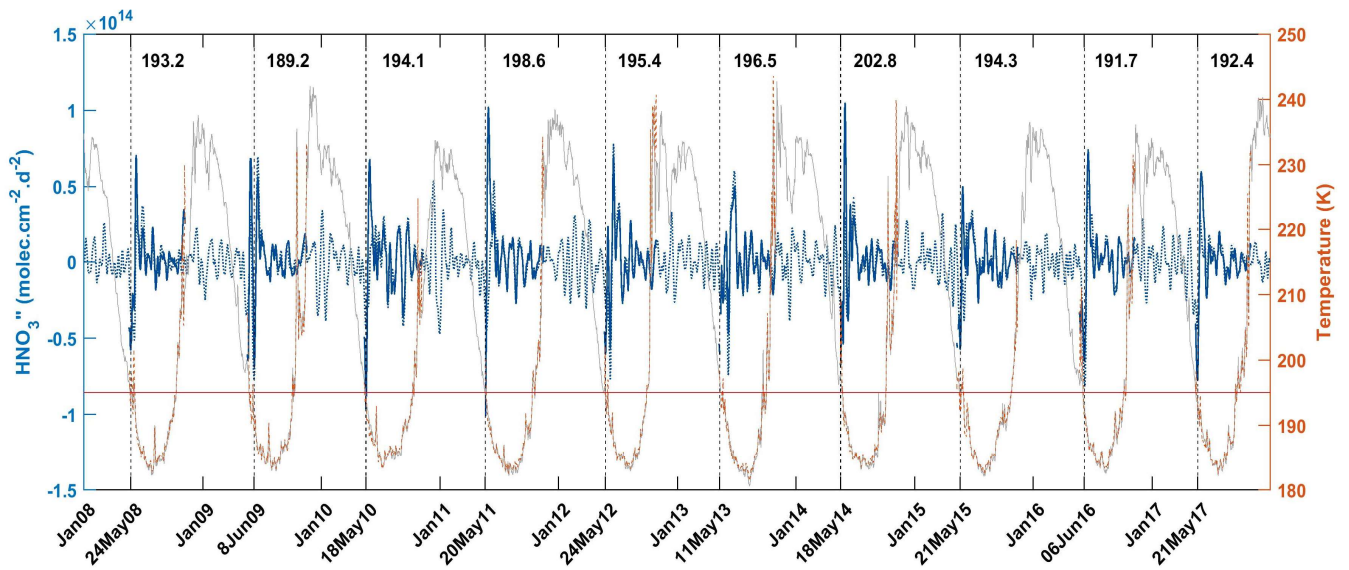
501
 502
 503
 504
 505
 506
 507
 508
 509
 510
 511
 512
 513
 514
 515
 516

Figure 2. Time series of daily IASI total HNO₃ column (blue) co-located with MLS and of MLS total HNO₃ columns (orange) within 2.5°x2.5° grid boxes, averaged in the 70°S–90°S (top panel) and the 50°S–70°S (bottom panel) equivalent latitude bands. Note that the MLS total column estimates were obtained by extending the MLS partial stratospheric column values using the FORLI-HNO₃ a priori information (see text for details). The error bars (blue) represent 3σ, where σ is the standard deviation around the IASI HNO₃ daily average.



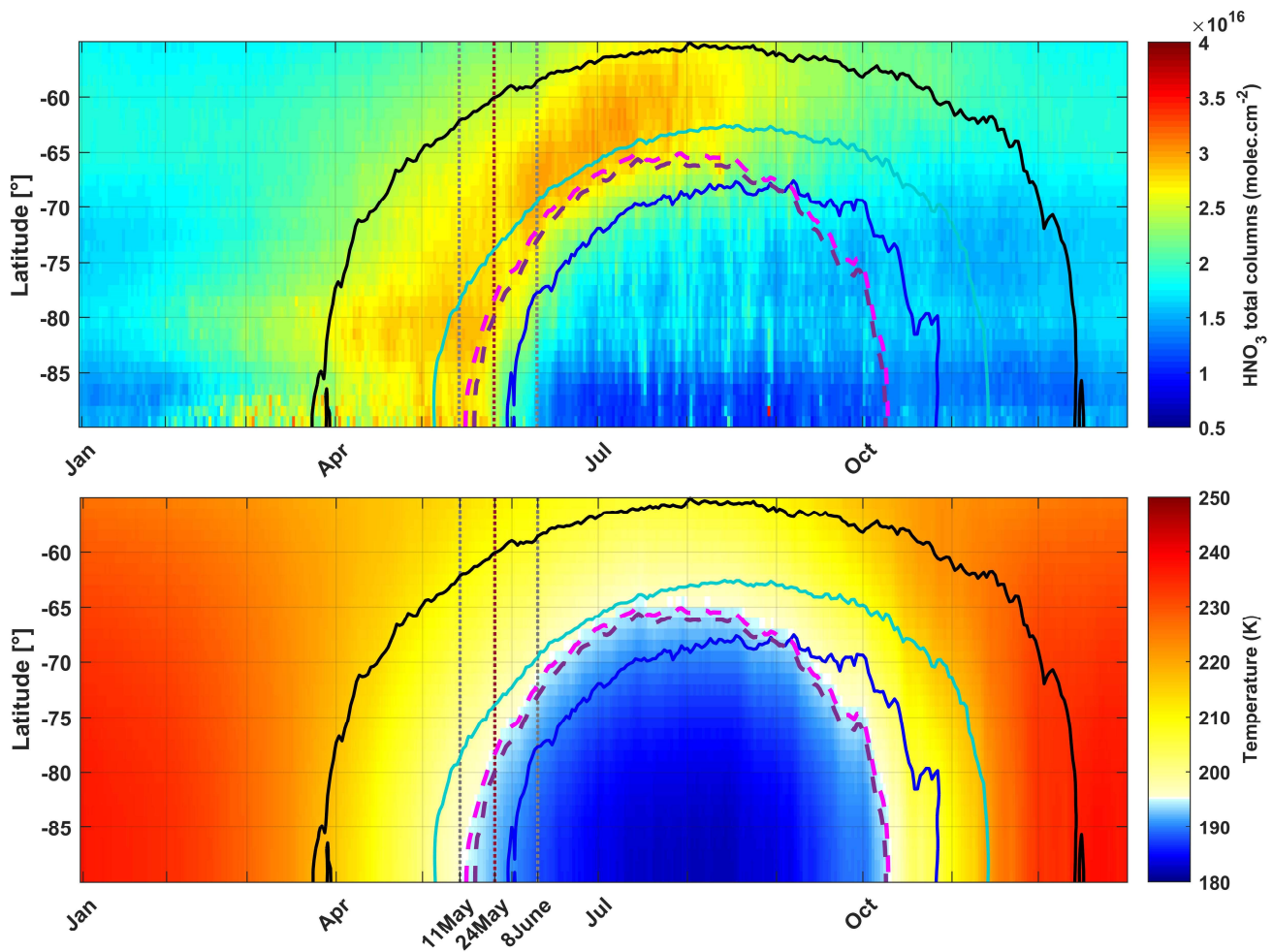
517
 518
 519
 520
 521
 522
 523
 524
 525
 526
 527
 528
 529
 530
 531
 532
 533
 534

Figure 3. (a) Time series of daily averaged HNO₃ total columns (solid lines) and temperatures taken at 50 hPa (dashed lines) in the 70° - 90° S equivalent latitude band, for the years 2008 – 2017. The green dotted line represents the temperatures at 20 hPa for the year 2010. (b) HNO₃ total columns versus temperatures (at 50 hPa) histogram during the year 2011, over the whole year (top) and for the 3 defined regimes (R1 - R3) separated in (a). The colors refer to the number of gridded measurements in each cell. (c) Evolution of daily averaged HNO₃ total columns with the highest occurrence (in bins of 0.1×10¹⁶ molec.cm⁻² and 2 K) as a function of the 50 hPa temperature for the years 2008 – 2017. The orange horizontal or vertical lines represent the 195 K threshold temperature.



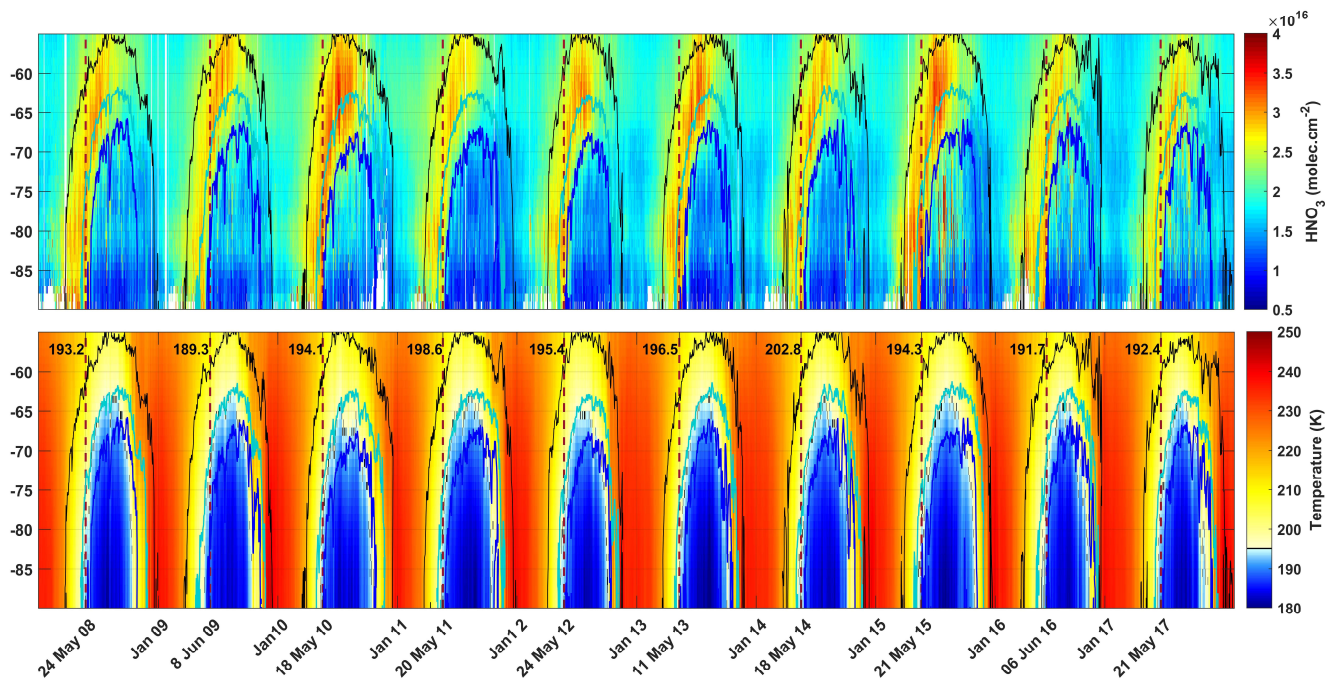
535
 536
 537
 538
 539
 540
 541
 542
 543
 544
 545
 546
 547
 548

Figure 4. Time series of total HNO₃ second derivative (blue, left y-axis) and of the 50 hPa temperature (red, right y-axis), in the region of potential vorticity at 530 K lower than $-10 \times 10^{-5} \text{ K} \cdot \text{m}^2 \cdot \text{kg}^{-1} \cdot \text{s}^{-1}$. The red horizontal line corresponds to the 195 K temperature. The vertical dashed lines indicate the second derivative minimum in HNO₃ for each year. The corresponding dates (in bold, on the x-axis) and temperatures are also indicated. The time series of total HNO₃ second derivative (dashed blue) and of temperature (grey) in the 70° – 90° S eqlat band are also represented.



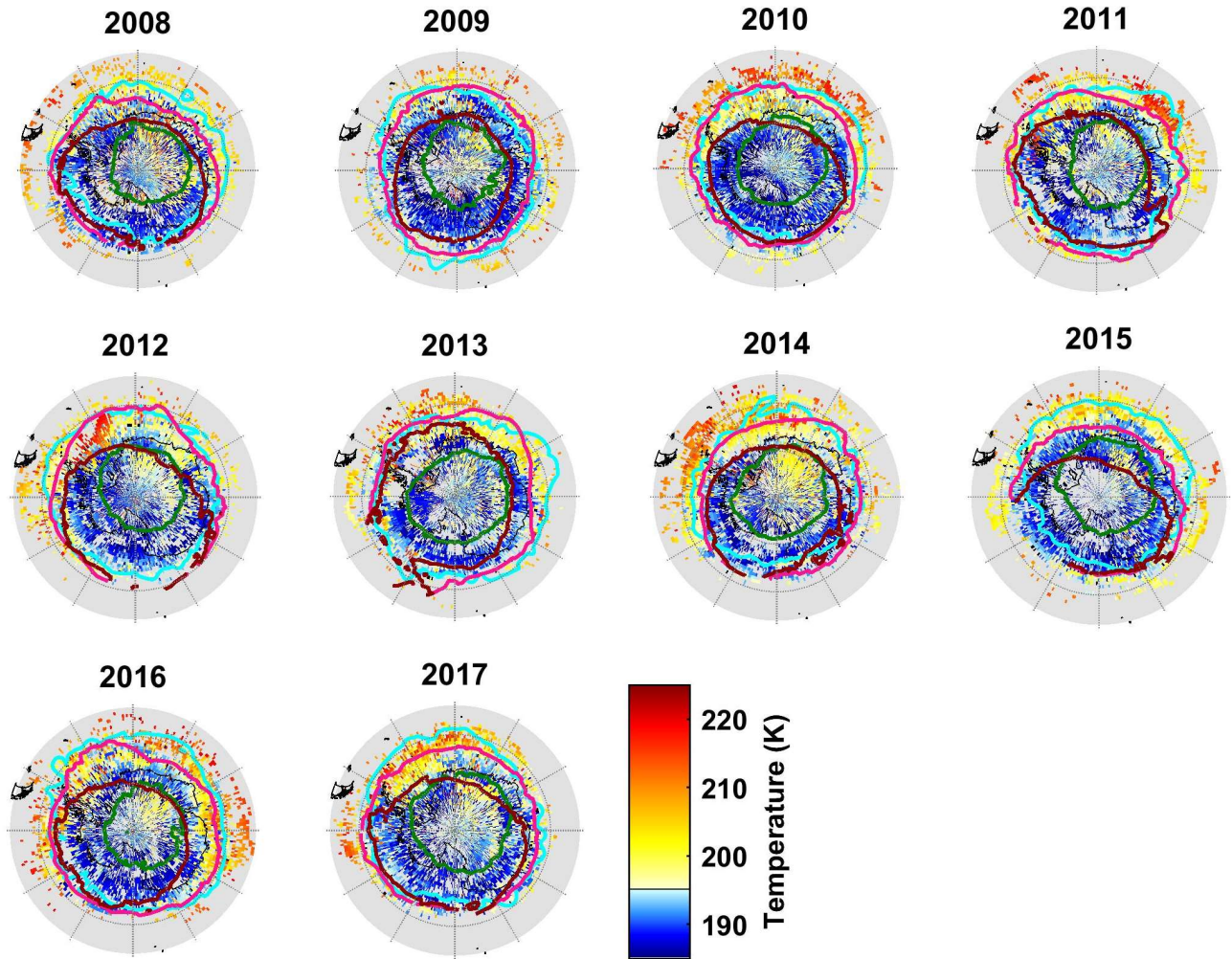
549
 550
 551
 552
 553
 554
 555
 556
 557
 558
 559

Figure 5. Zonal distributions of (a) HNO_3 total columns (in molec.cm^{-2}) from IASI and (b) temperatures at 50 hPa from ERA Interim (in K) in the 55°S to 90°S geographical latitude band and averaged over the years 2008 – 2017. Three isocontours for the climatological (2008-2017) and zonally averaged PV of -5 (black), -8 (cyan) and -10 (blue) ($\times 10^{-5} \text{K.m}^2.\text{kg}^{-1}.\text{s}^{-1}$) at 530 K, as well as the isocontours for the 195 K climatological (2008-2017) zonally averaged temperature (pink) and for the averaged 194.2 K drop temperature (purple) at 50 hPa are superimposed. The vertical grey dashed lines mark the earliest and latest dates for the averaged drop temperature in the 10-year IASI record and the red one indicates the average date for the drop temperatures calculated in the area delimited by the $-10 \times 10^{-5} \text{K.m}^2.\text{kg}^{-1}.\text{s}^{-1}$ PV contour.



560
 561
 562
 563
 564
 565
 566
 567
 568

Figure 6. Zonally averaged distributions of (top) HNO₃ total columns (in molec.cm⁻²) from IASI and (bottom) temperatures at 50 hPa from ERA Interim (in K). The geographical latitude range is from 55° to 90° south and the isocontours are PVs of -5 (black), -8 (cyan) and -10 (blue) (× 10⁻⁵ K.m².kg⁻¹.s⁻¹ at 530 K). The vertical red dashed lines correspond to the second derivative minima each year in the area delimited by a -10×10⁻⁵ K.m².kg⁻¹.s⁻¹ PV contour.



569
570
571
572
573
574
575
576
577
578
579
580
581
582
583
584
585
586
587

Figure 7. Spatial distribution ($1^\circ \times 1^\circ$) of the drop temperature at 50 hPa (K) (calculated from the total HNO_3 second derivative minima) for each year of IASI (2008–2017), in a region defined by a PV of $-8 \times 10^{-5} \text{ K} \cdot \text{m}^2 \cdot \text{kg}^{-1} \cdot \text{s}^{-1}$. The isocontours of $-10 \times 10^{-5} \text{ K} \cdot \text{m}^2 \cdot \text{kg}^{-1} \cdot \text{s}^{-1}$ at 530 K for the averaged PV (in green) and the minimum PV (in cyan) encountered over the period 10 May –15 July for each year and the isocontours of 195 K at 50 hPa for the averaged (in red) and the minimum (in pink) temperatures over the same period are represented.

588
589
590
591
592
593
594
595
596
597
598
599
600
601
602
603
604
605
606
607
608
609
610
611
612
613
614
615
616
617
618
619
620
621
622
623
624
625
626
627
628
629
630
631
632
633
634
635
636
637
638
639
640
641
642
643
644
645

References

- Braun, M., Groöß, J.-U., Woiwode, W., Johansson, S., Höpfner, M., Friedl-Vallon, F., Oelhaf, H., Preusse, P., Ungermann, J., Sinnhuber, B.-M., Ziereis, H., and Braesicke, P.: Nitrification of the lowermost stratosphere during the exceptionally cold Arctic winter 2015/16, *Atmospheric Chemistry and Physics Discussions*, <https://doi.org/10.5194/acp-2019-108>, 2019.
- Carslaw, K. S., Luo, B. P., and Peter, T.: An analytical expression for the composition of aqueous {HNO₃-H₂SO₄-H₂O} stratospheric aerosols including gas phase removal of HNO₃, *Geophys. Res. Lett.*, 22, 1877–1880, <https://doi.org/10.1029/95GL01668>, 1995.
- Carslaw, K. S., Wirth, M., Tsias, A., Luo, B. P., Dörnbrack, A., Leutbecher, M., Volkert, H., Renger, W., Bacmeister, J. T., Reimer, E., and Peter, T.: Increased stratospheric ozone depletion due to mountain-induced atmospheric waves, *Nature*, 391, 675–678, <https://doi.org/10.1038/35589>, 1998.
- Clerbaux, C., Boynard, A., Clarisse, L., George, M., Hadji-Lazaro, J., Herbin, H., Hurtmans, D., Pommier, M., Razavi, A., Turquety, S., Wespes, C., and Coheur, P.-F.: Monitoring of atmospheric composition using the thermal infrared IASI/MetOp sounder, *Atmospheric Chemistry and Physics*, 9, 6041–6054, <https://doi.org/10.5194/acp-9-6041-2009>, 2009.
- de Laat, A. T. J. and van Weele, M.: The 2010 Antarctic ozone hole: Observed reduction in ozone destruction by minor sudden stratospheric warmings, *Scientific Reports*, 1, 38, <https://doi.org/10.1038/srep00038>, 2011.
- de Zafra, R. and Smyshlyaev, S. P.: On the formation of HNO₃ in the Antarctic mid to upper stratosphere in winter, *Journal of Geophysical Research*, 106, 23 115, <https://doi.org/10.1029/2000JD000314>, 2001.
- Groöß, J. U., Engel, I., Borrmann, S., Frey, W., Günther, G., Hoyle, C. R., Kivi, R., Luo, B. P., Mollenker, S., Peter, T., Pitts, M. C., Schlager, H., Stiller, G., Vömel, H., Walker, K. a., and Müller, R.: Nitric acid trihydrate nucleation and denitrification in the Arctic stratosphere, *Atmospheric Chemistry and Physics*, 14, 1055–1073, <https://doi.org/10.5194/acp-14-1055-2014>, 2014.
- Hanson, D. and Mauersberger, K.: Laboratory studies of the nitric acid trihydrate: Implications for the south polar stratosphere, *Geophysical Research Letters*, 15, 855–858, <https://doi.org/10.1029/GL015i008p00855>, 1988.
- Harris, N. R. P., Lehmann, R., Rex, M., and von der Gathen, P.: A closer look at Arctic ozone loss and polar stratospheric clouds, *Atmospheric Chemistry and Physics*, 10, 8499–8510, <https://doi.org/10.5194/acp-10-8499-2010>, 2010.
- Hilton, F., Armante, R., August, T., Barnett, C., Bouchard, A., Camy-Peyret, C., Capelle, V., Clarisse, L., Clerbaux, C., Coheur, P.-F., Collard, A., Crevoisier, C., Dufour, G., Edwards, D., Faijan, F., Fourrié, N., Gambacorta, A., Goldberg, M., Guidard, V., Hurtmans, D., Illingworth, S., Jacquinet-Husson, N., Kerzenmacher, T., Klaes, D., Lavanant, L., Masiello, G., Matricardi, M., McNally, A., Newman, S., Pavelin, E., Payan, S., Péquignot, E., Peyridieu, S., Phulpin, T., Remedios, J., Schlüssel, P., Serio, C., Strow, L., Stubenrauch, C., Taylor, J., Tobin, D., Wolf, W., and Zhou, D.: Hyperspectral Earth Observation from IASI: Five Years of Accomplishments, *Bulletin of the American Meteorological Society*, 93, 347–370, <https://doi.org/10.1175/BAMS-D-11-00027.1>, 2012.
- Hoffmann, L., Spang, R., Orr, A., Alexander, M. J., Holt, L. A., and Stein, O.: A decadal satellite record of gravity wave activity in the lower stratosphere to study polar stratospheric cloud formation, *Atmospheric Chemistry and Physics*, 17, 2901–2920, <https://doi.org/10.5194/acp-17-2901-2017>, 2017.
- Höpfner, M., Luo, B. P., Massoli, P., Cairo, F., Spang, R., Snels, M., Di Donfrancesco, G., Stiller, G., von Clarmann, T., Fischer, H., and Biermann, U.: Spectroscopic evidence for NAT, STS, and ice in MIPAS infrared limb emission measurements of polar stratospheric clouds, *Atmospheric Chemistry and Physics*, 6, 1201–1219, <https://doi.org/10.5194/acp-6-1201-2006>, 2006.
- Höpfner, M., Pitts, M. C., and Poole, L. R.: Comparison between CALIPSO and MIPAS observations of polar stratospheric clouds, *Journal of Geophysical Research Atmospheres*, 114, 1–15, <https://doi.org/10.1029/2009JDO12114>, 2009.
- Hoyle, C. R., Engel, I., Luo, B. P., Pitts, M. C., Poole, L. R., Groöß, J. U., and Peter, T.: Heterogeneous formation of polar stratospheric clouds- Part 1: Nucleation of nitric acid trihydrate (NAT), *Atmospheric Chemistry and Physics*, 13, 9577–9595, <https://doi.org/10.5194/acp-13-9577-2013>, 2013.

646
647 Hurtmans, D., Coheur, P.-F., Wespes, C., Clarisse, L., Scharf, O., Clerbaux, C., Hadji-Lazaro, J., George, M., and Turquety,
648 S.: FORLI radiative transfer and retrieval code for IASI, *Journal of Quantitative Spectroscopy and Radiative Transfer*, 113,
649 1391–1408, <https://doi.org/10.1016/j.jqsrt.2012.02.036>, 2012.

650
651 James, A. D., Brooke, J. S. A., Mangan, T. P., Whale, T. F., Plane, J. M. C., and Murray, B. J.: Nucleation of nitric acid
652 hydrates in polar stratospheric clouds by meteoric material, *Atmospheric Chemistry and Physics*, 18, 4519–4531,
653 <https://doi.org/10.5194/acp-18-4519-2018>, 2018.

654
655 Keys, J. G., Johnston, P. V., Blatherwick, R. D., and Murcray, F. J.: Evidence for heterogeneous reactions in the Antarctic
656 autumn stratosphere, *Nature*, 361, 49–51, <https://doi.org/10.1038/361049a0>, 1993.

657
658 Klekociuk, A., Tully, M., Alexander, S., Dargaville, R., Deschamps, L., Fraser, P., Gies, H., Henderson, S., Javorniczky, J.,
659 Krummel, P., Petelina, S., Shanklin, J., Siddaway, J., and Stone, K.: The Antarctic ozone hole during 2010, *Australian
660 Meteorological and Oceanographic Journal*, 61, 253–267, <https://doi.org/10.22499/2.6104.006>, 2011.

661
662 Koop, T., Luo, B., Tsias, A., and Peter, T.: Water activity as the determinant for homogeneous ice nucleation in aqueous
663 solutions, *Nature*, 406, 611–614, <https://doi.org/10.1038/35020537>, 2000.

664
665 Lambert, A., Santee, M. L., Wu, D. L., and Chae, J. H.: A-train CALIOP and MLS observations of early winter Antarctic
666 polar stratospheric clouds and nitric acid in 2008, *Atmospheric Chemistry and Physics*, 12, 2899–2931,
667 <https://doi.org/10.5194/acp-12-2899-2012>, 2012.

668
669 Lambert, A., Santee, M. L., and Livesey, N. J.: Interannual variations of early winter Antarctic polar stratospheric cloud
670 formation and nitric acid observed by CALIOP and MLS, *Atmospheric Chemistry and Physics*, 16, 15 219–15 246,
671 <https://doi.org/10.5194/acp-16-15219-2016>, 2016.

672
673 Lambert, A. and Santee, M. L.: Accuracy and precision of polar lower stratospheric temperatures from reanalyses evaluated
674 from A-Train CALIOP and MLS, COSMIC GPS RO, and the equilibrium thermodynamics of supercooled ternary solutions
675 and ice clouds, *Atmospheric Chemistry and Physics*, 18, 1945–1975, <https://doi.org/10.5194/acp-18-1945-2018>, 2018.

676
677 Lowe, D. and MacKenzie, A. R.: Polar stratospheric cloud microphysics and chemistry, *Journal of Atmospheric and Solar-
678 Terrestrial Physics*, 70, 13–40, <https://doi.org/10.1016/j.jastp.2007.09.011>, 2008.

679
680 Molleker, S., Borrmann, S., Schlager, H., Luo, B., Frey, W., Klingebiel, M., Weigel, R., Ebert, M., Mitev, V., Matthey, R.,
681 Woiwode, W., Oelhaf, H., Dörnbrack, A., Stratmann, G., Groß, J.-U., Günther, G., Vogel, B., Müller, R., Krämer, M.,
682 Meyer, J., and Cairo, F.: Microphysical properties of synoptic-scale polar stratospheric clouds: in situ measurements of
683 unexpectedly large HNO₃-containing particles in the Arctic vortex, *Atmospheric Chemistry and Physics*, 14, 10 785–10 801,
684 <https://doi.org/10.5194/acp-14-10785-2014>, 2014.

685
686 Murphy, D. M. and Koop, T.: Review of the vapour pressures of ice and supercooled water for atmospheric applications,
687 *Quarterly Journal of the Royal Meteorological Society*, 131, 1539–1565, <https://doi.org/10.1256/qj.04.94>, 2005.

688
689 Peter, T.: Microphysics and heterogeneous chemistry of polar stratospheric clouds, *Annual Review of Physical Chemistry*,
690 48, 785–822, <https://doi.org/10.1146/annurev.physchem.48.1.785>, 1997.

691
692 Peter, T. and Groß, J.-U.: Chapter 4. Polar Stratospheric Clouds and Sulfate Aerosol Particles: Microphysics, Denitrification
693 and Heterogeneous Chemistry, in: *Stratospheric Ozone Depletion and Climate Change*, pp. 108–144, Royal Society of
694 Chemistry, <https://doi.org/10.1039/9781849733182-00108>, 2012.

695
696 Piccolo, C. and Dudhia, A.: Precision validation of MIPAS-Envisat products, *Atmospheric Chemistry and Physics*, 7, 1915–
697 1923, <https://doi.org/10.5194/acp-7-1915-2007>, 2007.

698
699 Pitts, M. C., Poole, L. R., Dörnbrack, A., and Thomason, L. W.: The 2009–2010 Arctic polar stratospheric cloud season: A
700 CALIPSO perspective, *Atmospheric Chemistry and Physics*, 11, 2161–2177, <https://doi.org/10.5194/acp-11-2161-2011>,
701 2011.

702

703 Pitts, M. C., Poole, L. R., Lambert, A., and Thomason, L.W.: An assessment of CALIOP polar stratospheric cloud
704 composition classification, *Atmospheric Chemistry and Physics*, 13, 2975–2988, <https://doi.org/10.5194/acp-13-2975-2013>,
705 2013.
706
707 Pitts, M. C., Poole, L. R., and Gonzalez, R.: Polar stratospheric cloud climatology based on CALIPSO spaceborne lidar
708 measurements from 2006 to 2017, *Atmospheric Chemistry and Physics*, 18, 10 881–10 913, <https://doi.org/10.5194/acp-18-10881-2018>, 2018.
709
710
711 Rodgers, C. D.: *Inverse Methods for Atmospheric Sounding - Theory and Practice*, vol. 2 of Series on Atmospheric Oceanic
712 and Planetary Physics, World Scientific Publishing Co. Pte. Ltd., <https://doi.org/10.1142/9789812813718>, 2000.
713
714 Roscoe, H. K., Feng, W., Chipperfield, M. P., Trainic, M., and Shuckburgh, E. F.: The existence of the edge region of the
715 Antarctic stratospheric vortex, *J. Geophys. Res.*, 117, D04301, doi:10.1029/2011JD015940, 2012.
716
717 Ronsmans, G., Langerock, B., Wespes, C., Hannigan, J. W., Hase, F., Kerzenmacher, T., Mahieu, E., Schneider, M., Smale,
718 D., Hurtmans, D., De Mazière, M., Clerbaux, C., and Coheur, P.-F.: First characterization and validation of FORLI-HNO₃
719 vertical profiles retrieved from IASI/Metop, *Atmospheric Measurement Techniques*, 9, 4783–4801,
720 <https://doi.org/10.5194/amt-9-4783-2016>, 2016.
721
722 Ronsmans, G., Wespes, C., Hurtmans, D., Clerbaux, C., and Coheur, P.-F.: Spatio-temporal variations of nitric acid total
723 columns from 9 years of IASI measurements – a driver study, *Atmospheric Chemistry and Physics*, 18, 4403–4423,
724 <https://doi.org/10.5194/acp-18-4403-2018>, 2018.
725
726 Santee, M. L., Manney, G. L., Froidevaux, L., Read, W. G., and Waters, J. W.: Six years of UARS Microwave Limb Sounder
727 HNO₃ observations : Seasonal, interhemispheric, and interannual variations in the lower stratosphere, *Journal of Geophysical*
728 *Research*, 104, 8225–8246, <https://doi.org/10.1029/1998JD100089>, 1999.
729
730 Santee, M. L., Lambert, A., Read, W. G., Livesey, N. J., Cofield, R. E., Cuddy, D. T., Daffer, W. H., Drouin, B. J., Froidevaux,
731 L., Fuller, R. A., Jarnot, R. F., Knosp, B. W., Manney, G. L., Perun, V. S., Snyder, W. V., Stek, P. C., Thurstans, R. P.,
732 Wagner, P. A., Waters, J. W., Muscari, G., de Zafra, R. L., Dibb, J. E., Fahey, D. W., Popp, P. J., Marcy, T. P., Jucks, K. W.,
733 Toon, G. C., Stachnik, R. A., Bernath, P. F., Boone, C. D., Walker, K. A., Urban, J., and Murtagh, D.: Validation of the Aura
734 Microwave Limb Sounder HNO₃ measurements, *Journal of Geophysical Research*, 112, 1–22,
735 <https://doi.org/10.1029/2007JD008721>, 2007.
736
737 Schreiner, J., Voigt, C., Weisser, C., Kohlmann, A., Mauersberger, K., Deshler, T., Kröger, C., Rosen, J., Kjöme, N., Larsen,
738 N., Adriani, A., Cairo, F., Donfrancesco, G. D., Ovarlez, J., Ovarlez, H., and Dörnbrack, A.: Chemical , microphysical , and
739 optical properties of polar stratospheric clouds, *Journal of Geophysical Research*, 108, 1–10,
740 <https://doi.org/10.1029/2001JD000825>, 2003.
741
742 Sheese, P. E., Walker, K. A., Boone, C. D., Bernath, P. F., Froidevaux, L., Funke, B., Raspollini, P., and von Clarmann, T.:
743 ACE-FTS ozone, water vapour, nitrous oxide, nitric acid, and carbon monoxide profile comparisons with MIPAS and MLS,
744 *Journal of Quantitative Spectroscopy and Radiative Transfer*, 186, 63–80, <https://doi.org/10.1016/j.jqsrt.2016.06.026>, 2017.
745
746 Snels, M., Scoccione, A., Liberto, L. D., Colao, F., Pitts, M., Poole, L., Deshler, T., Cairo, F., Cagnazzo, C., and Fierli, F.:
747 Comparison of Antarctic polar stratospheric cloud observations by ground-based and space-borne lidar and relevance for
748 chemistry–climate models, *Atmospheric Chemistry and Physics*, 19, 955–972, <https://doi.org/10.5194/acp-19-955-2019>,
749 2019.
750
751 Solomon, S.: Stratospheric ozone depletion: A review of concepts and history, *Reviews of Geophysics*, 37, 275–316,
752 <https://doi.org/10.1029/1999RG900008>, 1999.
753
754 Spang, R., Hoffmann, L., Höpfner, M., Griessbach, S., Müller, R., Pitts, M. C., Orr, A. M. W., and Riese, M.: A multi-
755 wavelength classification method for polar stratospheric cloud types using infrared limb spectra, *Atmospheric Measurement*
756 *Techniques*, 9, 3619–3639, <https://doi.org/10.5194/amt-9-3619-2016>, 2016.
757
758 Spang, R., Hoffmann, L., Müller, R., Groß, J.-U., Tritscher, I., Höpfner, M., Pitts, M., Orr, A., and Riese, M.: A climatology
759 of polar stratospheric cloud composition between 2002 and 2012 based on MIPAS/Envisat observations, *Atmospheric*
760 *Chemistry and Physics*, 18, 5089–5113, <https://doi.org/10.5194/acp-18-5089-2018>, 2018.

761
762 Toon, O. B., Hamill, P., Turco, R. P., and Pinto, J.: Condensation of HNO₃ and HCl in the winter polar stratospheres,
763 Geophysical Research Letters, 13, 1284–1287, <https://doi.org/10.1029/GL013i012p01284>, 1986.
764
765 Tritscher, I., Pitts, M. C., Poole, L. R., Alexander, S. P., Cairo, F., Chipperfield, M. P., et al.: Polar stratospheric clouds:
766 Satellite observations, processes, and role in ozone depletion, *Reviews of Geophysics*, 59, e2020RG000702,
767 <https://doi.org/10.1029/2020RG000702>.
768
769 Urban, J., Pommier, M., Murtagh, D. P., Santee, M. L., and Orsolini, Y. J.: Nitric acid in the stratosphere based on Odin
770 observations from 2001 to 2009 – Part 1: A global climatology, *Atmospheric Chemistry and Physics*, 9, 7031–7044,
771 <https://doi.org/10.5194/acp-9-7031-2009>, 2009.
772
773 Voigt, C., Schreiner, J., Kohlmann, A., Zink, P., Mauersberger, K., Larsen, N., Deshler, T., Kro, C., Rosen, J., Adriani, A.,
774 Cairo, F., Donfrancesco, G. D., Viterbini, M., Ovarlez, J., Ovarlez, H., and David, C.: Nitric Acid Trihydrate (NAT) in Polar
775 Stratospheric Clouds, *Science*, 290, 1756–1758, <https://doi.org/10.1126/science.290.5497.1756>, 2000.
776
777 Voigt, C., Larsen, N., Deshler, T., et al.: In situ mountainwave polar stratospheric cloud measurements: Implications for nitric
778 acid trihydrate formation, *J. Geophys. Res.*, 108(D5), doi:10.1029/2001JD001185, 2003.
779
780 Voigt, C., Schlager, H., Luo, B. P., Dörnbrack, A., Roiger, A., Stock, P., Curtius, J., Vössing, H., Borrmann, S., Davies, S.,
781 Konopka, P., Schiller, C., Shur, G., and Peter, T.: Nitric Acid Trihydrate (NAT) formation at low NAT supersaturation in
782 Polar Stratospheric Clouds (PSCs), *Atmospheric Chemistry and Physics*, 5, 1371–1380, [https://doi.org/10.5194/acp-5-1371-](https://doi.org/10.5194/acp-5-1371-2005)
783 2005, 2005.
784
785 von König, M.: Using gas-phase nitric acid as an indicator of PSC composition, *Journal of Geophysical Research*, 107,
786 <https://doi.org/10.1029/2001jd001041>, 2002.
787
788 Wang, X. and Michelangeli, D. V.: A review of polar stratospheric cloud formation, *China Particuology*, 4, 261–271,
789 [https://doi.org/10.1016/S1672-2515\(07\)60275-9](https://doi.org/10.1016/S1672-2515(07)60275-9), 2006.
790
791 Wegner, T., Groß, J.-U., von Hobe, M., Stroh, F., Sumin'ska-Ebersoldt, O., Volk, C. M., Hösen, E., Mitev, V., Shur, G.,
792 and Müller, R.: Heterogeneous chlorine activation on stratospheric aerosols and clouds in the Arctic polar vortex,
793 *Atmospheric Chemistry and Physics*, 12, 11 095–11 106, <https://doi.org/10.5194/acp-12-11095-2012>, 2012.
794
795 Wespes, C., Hurtmans, D., Clerbaux, C., and Coheur, P.-F.: O₃ variability in the troposphere as observed by IASI over 2008–
796 2016: Contribution of atmospheric chemistry and dynamics, *Journal of Geophysical Research: Atmospheres*, 122, 2429–
797 2451, <https://doi.org/10.1002/2016JD025875>, <http://doi.wiley.com/10.1002/2016JD025875>, 2017.
798
799 WMO: Scientific Assessment of Ozone Depletion: 2014, Global Ozone Research and Monitoring Project – Report No. 55,
800 World Meteorological Organization, Geneva, Switzerland, 2014.
801
802 Zhu, Y., Toon, O. B., Lambert, A., Kinnison, D. E., Brakebusch, M., Bardeen, C. G., Mills, M. J., and English, J. M.:
803 Development of a Polar Stratospheric Cloud Model within the Community Earth System Model using constraints on Type I
804 PSCs from the 2010-2011 Arctic winter, *Journal of Advances in Modeling Earth Systems*, 7, 551–585,
805 <https://doi.org/10.1002/2015ms000427>, 2015.
806
807 Zondlo, M. A., P. K. Hudson, A. J. Prenni, and M. A. Tolbert: Chemistry and microphysics of polar stratospheric clouds and
808 cirrus clouds, *Annu. Rev. Phys. Chem.*, 51, 473–499, 2000.